Thermally Induced Oxygen Related Defects in Eco-friendly $ZnFe_2O_4$ Nanoparticles for Enhanced Wastewater Treatment Efficiencies

Basma Al-Najar[a*], Adnan Younis[a], Layla Hazeem[b], Shama Sehar[b], Suad Rashdan[c], M. Nasiruzzaman Shaikh[d], Hanan Albuflasa[a] and Nicholas P.Hankins[e]

[a]Department of Physics, College of Science, University of Bahrain, P.O. Box 32038, Sakhir Campus, Kingdom of Bahrain

[b]Department of Biology, College of Science, University of Bahrain, P.O. Box 32038, Sakhir Campus, Kingdom of Bahrain

[c]Department of Chemistry, College of Science, University of Bahrain, P.O. Box 32038, Sakhir Campus, Kingdom of Bahrain

[d]Interdisciplinary Research Center for Hydrogen and Energy Storage (IRC-HES), King Fahd University of Petroleum and Minerals (KFUPM), Dhahran, Saudi Arabia

[e]Department of Engineering Science, The University of Oxford, Parks Road, OX3 1PJ Oxford, UK

[*]Corresponding Author: balnajar@uob.edu.bh

Abstract

Herein, a simple but highly effective strategy of thermal annealing to modulate oxygen vacancies related defects in $ZnFe_2O_4$ (ZFO) nanoparticles for obtaining enhanced wastewater treatment efficiencies is reported. The as-prepared nanoparticles were thermally annealed at three different temperatures (500 °C, 600 °C and 700 °C) and their phase purity was confirmed by X-ray diffraction (XRD). All samples were found to exhibit pure phases of ZFO with different crystallite sizes ranging from 10 nm to 25 nm. The transmission electron microscope (TEM) images showed well dispersed nanoparticles and a strong correlation of grain size growth with annealing temperature was established. The optical absorption and emission characteristics were estimated through UV-visible and Photoluminescence (PL) spectroscopy. Raman spectroscopy and X-ray Photoelectron Spectroscopy (XPS) confirmed the variation of oxygen vacancies in the synthesised samples' lattice. The photocatalytic activities of all samples were investigated and the highest efficiencies were recorded for the ZFO samples annealed at 500 °C. Under high salinity condition, the organic dye degradation efficiency of the same sample remained the highest among all. The excellent dye degradation abilities in ZFO samples can be attributed to the abundance of oxygen vacancies in the crystal lattice that slow down the recombination rate during the photocatalysis process. Moreover, cytotoxicity tests revealed that all prepared ZFO samples showed insignificant cell structure effects on *Picochlorum sp* microalgae, as verified by Fourier-transform infrared (FTIR) spectroscopy. On the other hand, no significant changes were detected on the viable cell concentration and *Chlorophyll a* content. This work presents a systematic way to finely tune the crystal sizes and to modulate oxygen related defects in ZFO through a simple but highly effective annealing

approach to signify their potential in industrial wastewater and seawater treatment processes.

Keywords:

Crystal size, Oxygen vacancies, Photocatalysis, Dye degradation, Cytotoxicity, *Picochlorum sp,*

1 Introduction

The scarcity of freshwater resources has been one of leading global environmental and sustainability challenges. Most of the fresh water and seawater resources (Al-Najar et al., 2020) are affected by human activities due to disposal of hazardous pollutants such as industrial dyes (Tkaczyk et al., 2020), heavy metals (Abdullah et al., 2020), antibiotics (J. Huang et al., 2020) and pesticides (Sert et al., 2017), which are harmful for ecosystem and human health (Qureshi, 2020). Various industries extensively used organic dyes for coloring and then dispose them directly into aqueous effluents, which in turn pollute natural water resources. Even a small concentration of these dyes in water prevents penetration of sunlight into water thus affecting the aquatic flora. Moreover, many dyes are carcinogenic, mutagenic and toxic to microorganisms and aquatic species (Chen et al., 2017; Hashemi et al., 2019; Sehar et al., 2021; Younis et al., 2018; Younis and Loucif, 2021) and their effective removal by transforming them into harmless products before release into the environment is of utmost importance. In high salinity conditions, the removal of these dyes become even harder because of the chemical complexity and the salt ions concentrations (T. Wang et al., 2017).

Various nanomaterials have been investigated in water treatment techniques due to their small size and controllable properties (controlling size – photocatalysis)(Sehar et al., 2019; Younis et al., 2016). In a typical photocatalysis process, a semiconducting material absorbs energy, which is directly related to the bandgap of the material and generate electron/hole pairs. The reactive species generated by the separation of electron/hole pairs interact with the dye molecules and convert them into less harmful inert products (e.g., water, carbon dioxide) (Chiu et al., 2019; Mahy et al., 2019). Titanium dioxide is considered as a flagship material that has been widely utilized as an efficient photocatalyst for so many years(Porcar-Santos et al., 2020). However, due to its large bandgap (~3.2 eV), it is only affective under ultra-violet (UV) light. It is highly desirable to achieve efficient photocatalytic degradation in visible light rather than in UV light, as visible light constitutes about 50% of solar radiation whereas, UV light forms only 4% (T. Wang et al., 2017). Therefore, the exploration of functional nanomaterials with relatively narrow bandgaps, that may have strong absorption in the visible region, is highly advantageous for obtaining excellent photocatalytic performance (Guo et al., 2014).

Spinel ferrites, owing to small bandgaps (less than 2.2 eV), possess a cubic structure with formula $(A)[B]_2O_4$, where (A) and [B] are tetrahedral and octahedral cation sites in an FCC anion (oxygen) sublattice. In bulk Zinc Ferrite ($ZnFe_2O_4$ (ZFO)), A and B cationic sites are occupied by Zn^{2+} and Fe^{3+} ions. On the other hand, the nanocrystalline ZFO system always shows up as a mixed spinel in which Zn^{2+} and Fe^{3+} ions are distributed over A and B-sites (Qin et al., 2017). The nanocrystalline ZFO could absorb visible range of solar radiation and provide numerous catalytic sites for adsorption, thus have a great potential of an efficient photocatalysts (Baynosa et al., 2020). ZFO is also known of its chemical stability, low cost and environmental friendliness(Sapna et al., 2019). The unique crystal structure of ZFO makes it highly reactive and responsive (Wu et al., 2019) besides the ability of controlling and tuning these properties to get the optimum efficiency for the desired application (Sun et al., 2020).

So far, pure ZFO have not been successfully demonstrated for efficient photocatalysis due to its high recombination rate between holes and electrons (Yentür and Dükkancı, 2020). Therefore, to overcome this drawback, heterostructure of ZFO with other functional materials have been implemented to demonstrate its potential in this field (Naseri et al., 2020). This mainly involved Graphene oxide (Chandel et al., 2020) and noble metals (Khadgi and Upreti, 2019) that have shown a great photocatalysis efficiency in comparison with pure ZFO. Consequently, this will add more economical and environmental hazard cost (Prasad et al., 2020; Wang et al., 2020) beside the multi-stage preparation routes and the need of the optimization between the absorption ability and the electron-hole yield within the heterogeneous structure (Serpone, 2018). Therefore, considering the photocatalytic activity of pure ZFO is still challenging, due to the complexity of photocatalytic relation to the crystal structure (crystal size and defects) of materials (Divya et al., 2020; Lei et al., 2020; Yadav et al., 2018).

In this work, we focused on the possibilities of tuning the defects concentration in pure ZFO nanoparticles by thermal annealing to investigate their photocatalytic efficiencies. The samples were post annealed at different temperatures (500^{o}C, 600^{o}C and 700^{o}C) which strongly influence crystal size and defects characteristics. Furthermore, the influence of ZFO crystal sizes on the photocatalytic activities were investigated in aqueous solution as well as in seawater. We also investigated the cytotoxicity of all ZFO samples on *Picoplankton*

Picochlorum sp micro algae in term of their structure, viable cells concentration, Reactive Oxidative Species (ROS) generation and their *chlorophyll a* content. This work may provide new insights for defects modulation in nanocrystalline ZFO to explore their potential as an effective catalyst for industrial wastewater treatment.

2 Materials and Methods

2.1 Synthesis of ZFO nanoparticles

The ZFO nanoparticles were synthesized by using sol-gel method and the whole process is schematically shown in **Figure 1.** For a typical chemical synthesis, equal amounts of citric acid and $Fe(NO_3)_3.9H_2O$ and 4g of $Zn(NO_3)_2$ were mixed with 1.2 L distilled water followed by magnetic stirring. After 25 min of stirring, around 15 ml of Ammonium Hydroxide was added to the solution to alter the pH to 7. Afterwards, the mixed solution was heated at 130 ºC along with continuous stirring until the solution is completely evaporated and burned into black powder (Rashdan and Hazeem, 2020). The as-prepared samples were annealed at 500 ºC, 600 ºC and 700 ºC for 30 minutes to obtain the ZFO crystalline structure. For simplicity, the annealed samples are renamed as ZFO-500, ZFO-600 and ZFO-700, respectively.

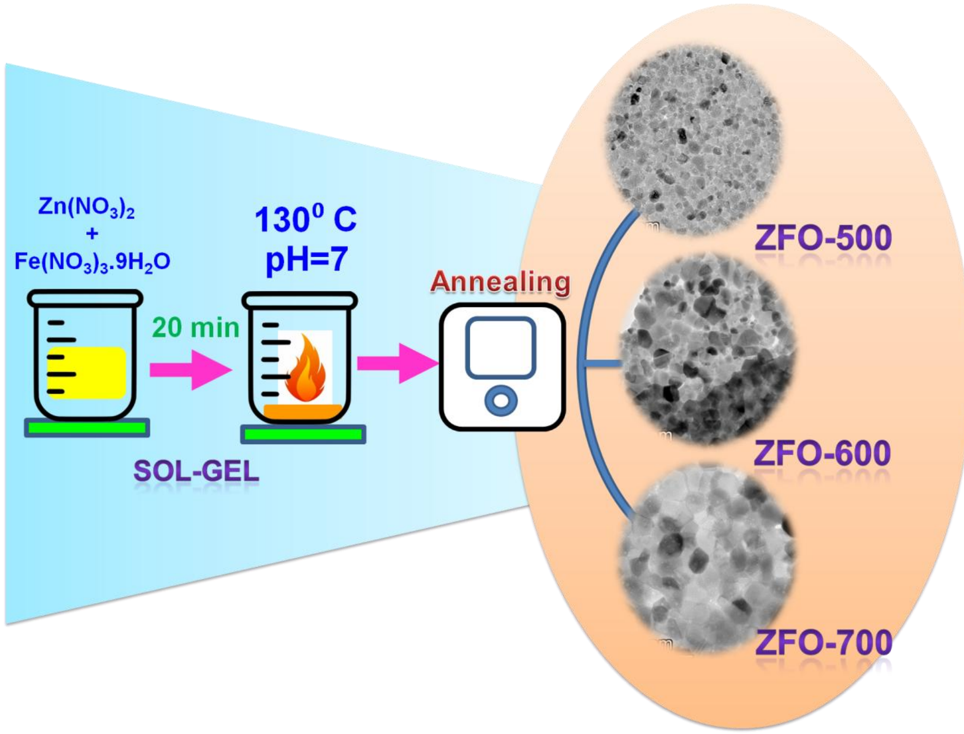

Figure 1: Schematic diagram showing step by step synthesis of ZFO nanoparticles.

2.2 Characterization of ZFO nanoparticles

The morphology and grain sizes of ZFO samples were determined by using Transmission Electron Microscopy (Talos L120C G2- LaB6). The chemical phase and crystallite structure were determined using X-ray diffraction (XRD) using Rigaku Uitima IV equipped with Cu-Kα radiation source (0.15418 nm) with angle ranging from 10^o to 80^o. Fourier-transform infrared spectroscopy (FTIR)- (Shimadzu- IRAffinity-1S) was used to investigate the infrared absorption of the samples and the sample/algae combination. Optical properties were investigated using UV-vis spectroscopy (Shimadzu-Lambda-4B), Photoluminescence Spectroscopy (PL) (Jasco, Spectrophotometer FP-8500, Xenon discharge lamp quartz cells [1cm]), Raman Spectroscopy and X-ray Photoelectron Spectroscopy (XPS). The N2 adsorption-desorption isotherm measurements were performed using a Micromeritics ChemiSorb 2750 and the Brunauer–Emmett–Teller (BET) technique with the degassing temperature of 300^{o} C for 180 min. The pore-size distribution (PSD) was obtained from the adsorption branch of the isotherms via the Barrett–Joyner–Halenda (BJH) method.

2.3 Photocatalytic Activities of ZFO nanoparticles

The photocatalytic activities of all samples were evaluated for the removal of methylene orange (MO) and methylene blue (MB) from aqueous solutions and seawater under solar simulated irradiation using solar simulation chamber- Xenoterm-1500RF, CCI (Spain) with Xenon lamp (1.5 kW). Conventionally, the photocatalytic reactions were carried out in a 20 mL photoreactor, which contained 100 mg/L of ZFO samples dispersed in 15 mg/L dyes solutions under the solar irradiation source. Prior to irradiation, the solutions were stirred for 30 minutes in the dark to assure attaining adsorption/desorption equilibrium. For determination of MO and MB decolorization, the absorbance of each sample was measured at different time intervals (each 10 min for 120 min) using UV 1800 PC spectrophotometer.

Degradation efficiency was calculated using the following equation:

$$D(\%) = \left(1 - \frac{C}{C_0}\right) \times 100 \qquad (1)$$

Where D is the degradation efficiency, C is the concentration of dye at a certain time and C_0 is the initial concentration of dye in solution.

Recyclability experiments were also conducted to check the stability of the synthesized ZFO samples as well as FTIR and XRD that applied after the photocatalysis process. To further investigate the photocatalysis process, the Total Organic Carbon (TOC) content in the MO and ZFO solution was measured with a Shimadzu SSM-5000-A carbon analyzer. Moreover, to monitor the Reactive Oxygen spices (ROS) related to the photocatalysis process of the MO dye, different scavengers were used; Benzoquinone (BQ) (6mmol/L, Ammonium Oxalate (AO)(0.05g/L), Catalase, (20mg/L), 2-proponol (0.1 mmol/L) and Potassium per Sulphate (KPS) (mmol/L) , in the dye solution.

2.4 Cytotoxcity Assay of ZFO nanoparticles

Biotoxicity assay of the prepared ZFO samples were conducted using *Picochlorum sp.* culture, which is one of the main microalgae found in high salinity marine environment. Pure culture samples were obtained from the National Mariculture Centre, Ministry of Municipalities and Urban Planning, Kingdom of Bahrain. *Picochlorum sp.* microalgea samples were sub-cultured in 2 L flask in filtered seawater and incubated under 18 ^{o}C. To assess the cytotoxicity effect of the prepared ZFO samples, all samples were added to the *Picochlorum sp*. culture samples at 50 mg/L, during exponential growth phase.

The Organization for Economic Cooperation and Development (OECD) 201 algal growth inhibition test guidelines were followed with some modification. The cultures were incubated with ZFO samples at exponential growth phase. The viable cell counts and measurements of *Chlorophyll a* concentrations were performed every week starting from the first day of inoculation of algae with ZFO samples for a total of 4 weeks. At the end of the 4 weeks period, ROS were measured for all algae/ZFO samples. FTIR analysis was also applied for the algae/ ZFO samples and compared with the control sample. MuseTM Cell analyzer (Millipore, USA) was applied to measure the viable cell counts and the ROS percentage. The MuseTM Cell analyzer applied miniaturized fluorescent detection and micro-capillary technology to deliver quantitative cell analysis of both suspension and adherent cells 2 to 60 μmin diameter. *Chlorophyll a* concentration for all control and ZFO/algae samples were measured using spectrophotometer (PerkinElmer UV spectrophotometer). The samples were prepared following the UNESCO protocol (Vohra 1966) as 30 mL of each ZFO/algae culture sample were collected and the Chlorophyll a was extracted using 90% acetone.

The ZFO-500 samples with different concentrations (0.5, 2.5, 5, 25 and 50 mg/L) were also tested. The viable cell counts were measured after 1 week of inoculation of algae with ZF-500 sample. Three replicates were applied for all cytotocity assay experiments. The data is displayed as mean ± standard deviation (SDEV). One- way analysis of variance (ANOVA) followed by Tukey's pairwise comparison using Minitab version 1.6 were applied to test any significance variation between the different treatments and the control. The level of significance was accepted at $p<0.05$ (Hazeem et al., 2016).

3 Results and Discussion

3.1 Morphology of ZFO nanoparticles

The morphology of ZFO samples prepared at different annealing temperatures was investigated using TEM and the results are depicted in **Figure 2**. The TEM images revealed a homogenous size distribution with semi-spherical grains for all prepared samples (ZFO-500, ZFO-600 and ZFO-700). A considerable particle size variation was recorded by changing annealing temperatures. The ZFO-500 sample possessed grains sizes with diameters ranging from 10-15 nm, which is the smallest range among all samples. The samples annealed at higher temperatures (ZFO-600 and ZFO-700) exhibited larger grain sizes ranging from 20-25 nm and 25-30 nm, respectively. For the sake of accuracy, the grain sizes were determined by counting sufficiently large number of grains. The high resolution transmission electron microscopy (HRTEM) images of all samples are depicted in the inset of **Figures 2a-2c**. The lattice fringes of all samples are clearly visible with d-spacing of 0.25 nm correspond to the (311) crystal plane of ZFO crystalline phase configuration. Such grain growth is attributed to the annealing temperature (Afzal et al., 2020; Amir et al., 2018), as higher annealing temperature creates volume expansion and super-saturation reduction to the crystal lattice system (Dippong et al., 2020, 2019). Thus, more grain boundaries related defects could be present in ZFO-500 sample as compared to others which can be reduced by increasing annealing temperature. Also, ZFO sample could have higher lattice grain strain which can inhibit grain growth and by annealing at higher temperatures, larger grains were formed as shown in **Figures 2b and 2c**.

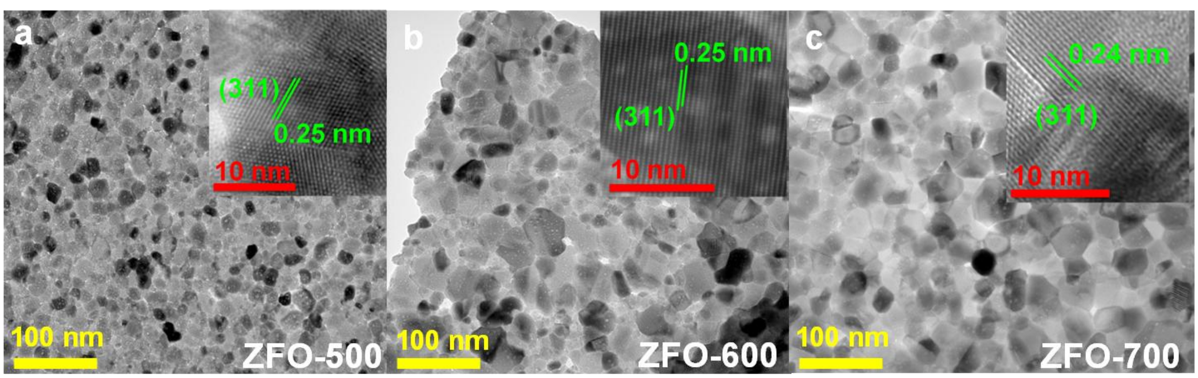

Figure 2: TEM images of ZFO nanoparticles prepared at **(a)** 500 ^oC, **(b)** 600 ^oC and **(c)** 700 ^oC annealing temperatures. In the inset, HRTEM images of individual nanoparticles are depicted.

3.2 Structural Properties of ZFO nanoparticles

The XRD spectra of as-prepared and annealed ZFO samples are depicted in **Figure 3a.** No well-defined peaks were found from the XRD spectrum of the as-prepared ZFO indicating its amorphous structure. When ZFO samples were annealed at 500, 600 and 700 ^oC, the crystal planes of cubic spinel phase of ZFO become clearly visible at (111), (220), (311), (222), (400), (422), (511), (440) and (533). Rietveld analysis of the XRD spectrum confirmed the formation of pure ZFO cubic spinel phase with space group Fd3m which matches well with JCPDS NO. 01-078-6543. From XRD results, the crystallite size, microstrain and lattice parameters of all samples were calculated and shown in **Table TS1.** For ZFO-600, a small peak emerged at around $2\theta = 32^o$ which was more obvious at ZFO-700 and could be related to an inconsequential Fe_2O_3 phase (Amiri et al., 2020; Surendra et al., 2020).

The crystalline size of ZFO was found to increase by thermal annealing and were recorded as 10 nm, 18 nm and 25 nm, for ZFO-500, ZFO-600 and ZFO-700, respectively (as shown in **Table TS1**). This increased crystallite size may be attributed to reduced macrostrain within crystal structure of ZFO which were calculated as 0.54, 0.28 and 0.21 for ZFO-500, ZFO-600 and ZFO-700, respectively. A slight decrease in lattice parameter from 8.4437 to 8.4404 was also recorded with annealing temperature. From our XRD and TEM results, it is well established now that annealing temperature can greatly influence grain growth and crystallite size in ZFO which are well accord to literature (Radhakrishnan et al., 2016). The XRD peaks broadening, smaller crystal size, high microstrain and larger lattice parameters of ZFO-500 compared to its counter parts may also indicate the existence of crystal lattice defects related to oxygen vacancies (Afzal et al., 2020). As annealing temperature increased from 500°C to 700 °C, the XRD peaks become sharper with higher intensity. Also, higher annealing temperature allows more oxygen to be involved in the crystal lattice structure, filling any possible vacancies and forming large and refined crystal structure (Jaffari et al., 2012) for the cubic ZFO spinel phase. During this refinement process, both Zn^{2+} and Fe^{3+} in the tetrahedral and octahedral sites cations may exchange positions (Mana et al., 2019). Such re-distribution of cations and crystal defects may decrease lattice parameter and microstrain (Amir et al., 2018; El-naggar et al., 2020).

The FTIR spectra of the annealed ZFO samples are shown in **Figure 3b.** All corresponding peaks of ferrite structure were clearly visible in all ZFO samples with no evidence of any impurity peaks. The spectrum consists of five main obvious peaks at v_1 = 450 cm^{-1}, v_2 = 547 cm^{-1}, v_3= 1612 cm^{-1} and v_4 = 2414 cm^{-1} and v_5 =3400 cm^{-1} which matches well with ferrite structures (Bhushan Das et al., 2021). The peaks v_1 and v_2 may be related to Fe-O and Zn-O stretching vibrations, which represent the metal bonding at tetrahedral site of the spinel ferrite structure. The peaks v_3, v_4 and v_5 represent the stretching and bending vibrations of H-O-H bands which represent water molecules bonding (Shah et al., 2021; Vinosha et al., 2017). When comparing the three ZFO spectra, v_2 and v_5 have shown a noticeable intensity increase in ZFO-500 sample. The increase in FTIR absorption peak intensity indicates changes in ZFO lattice structure in the form of oxygen related defects (Shah et al., 2021).

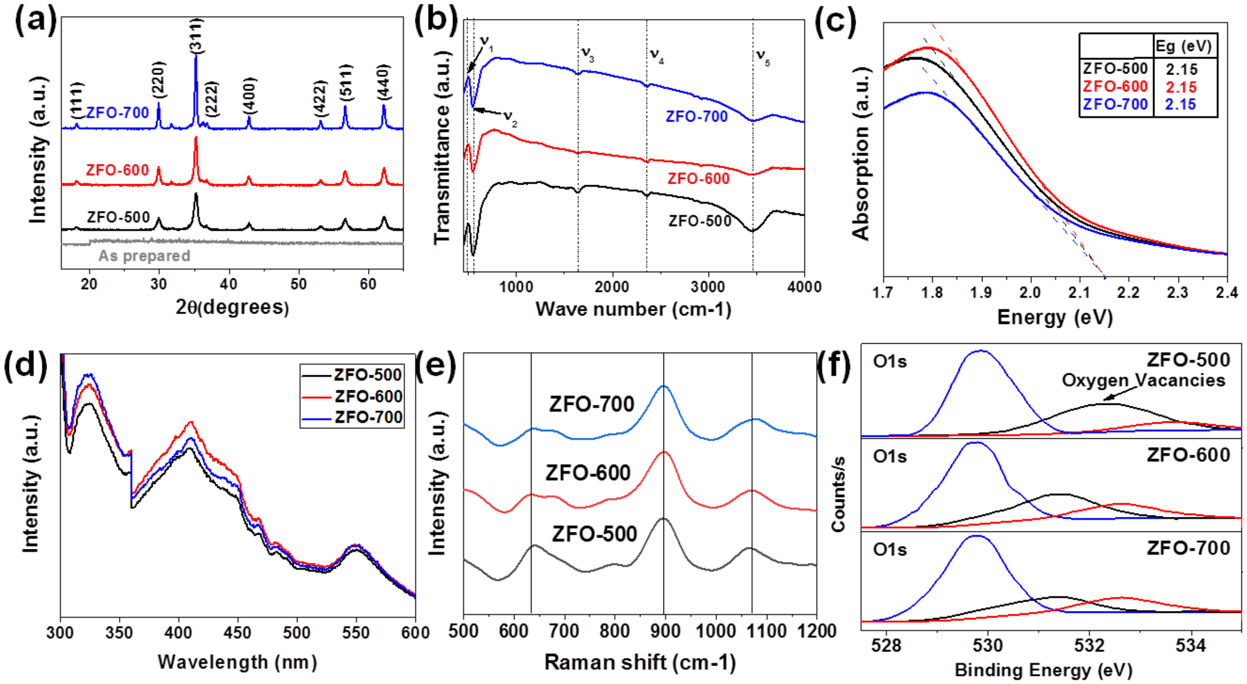

Figure 3: The characteristics of $ZnFe_2O_4$ samples prepared with different annealing temperatures (ZFO-500, ZFO-600 and ZFO-700) applying **(a)** X-ray Diffraction (XRD), **(b)** Fourier-transform infrared spectroscopy (FTIR) **(c)**UV-vis spectroscopy, and **(d)** The photoluminescence (PL) spectroscopy (e) Raman Spectroscopy (f) XPS spectroscopy (O1s).

3.3 Optical Properties of ZFO nanocrystals

The absorption spectra of all samples were analyzed using UV-vis spectrometer and they all showed similar patterns, where the main absorption region was found in between 200 and 450 nm. The bandgaps of all samples were calculated and no significant variation in their values were recorded as shown in **Figure 3c.**

Furthermore, photoluminescence (PL) emission spectroscopy was performed and all samples showed excitation wavelength at 410 nm (3.03 eV) and 550 nm (2.25 eV) as shown in **Figure 3d** which are well accord to literature (Dang et al., 2016; Manikandan et al., 2014). These excitation peaks can be related to the electronic levels between the conduction band (CB) and the valance band (VB). A lower PL peak intensity for ZFO-500 was found in comparison to ZFO-600 and ZFO-700, which may be associated to the hole-electron recombination. The lower peak intensity could be attributed to the lower recombination rate which is related to the oxygen defects in the crystal lattice of ZFO-500 (Younis et al., 2016) (Swathi et al., 2021). Therefore, ZFO-500 is anticipated to possess slow electron-hole recombination as compared to their counter parts.

To confirm the existence and variation of oxygen vacancies in the crystals of ZFO samples, Raman spectroscopy was performed as one of the sensitive modalities to the vibration of Oxygen ions (Deka et al., 2019; Fu et al., 2021; Sarkar and Khan, 2019). **Figure 3e** demonstrates the Raman spectra of ZFO-500, ZFO-600 and ZFO-700. Three peaks were distinguished for all samples at 630 cm^{-1}, 900 cm^{-1} and 1060 cm^{-1}. The only significant difference between the spectra of the three samples is in band 630 cm^{-1} where larger peak with higher amplitude is attributed to ZFO-500, which can be related to the abundance of oxygen vacancies. Previous reports related the stretching vibration change in Oxygen Raman band to oxygen vacancies in Zinc Ferrite (Arora and Sharma, 2021; Zhang et al., 2020). X-ray Photoelectron Spectroscopy (XPS) has been also applied widely to detect oxygen vacancies in ferrite crystal lattice (Peng et al., 2019; Sarkar and Khan, 2019; Swathi et al., 2021; J. Wang et al., 2019). The O1s fitted spectra of ZFO-500, ZFO-600 and ZFO-700 are shown in **Figure 3f**. The middle peak related to the binding energy 531.6 eV to 532 eV can be assigned to the oxygen vacancies in ZFO crystal lattice as shown in previous reports (Peng et al., 2019; Swathi et al., 2021; J. Wang et al., 2019)**.** The perceptible change in the ZFO-500 Os-1 spectra in comparison to ZFO-600 and ZFO-700 confirms the higher concentration of oxygen vacancies in ZFO-500 lattice, consisting with Raman and PL results.

3.4 Adsorption-Desorption isotherms

Adsorption-desorption isotherm hysteresis loops for ZFO nanoparticles are shown in **Figure 4a.** The isotherm curves of all samples exhibit similar behavior, where an elevated H4 type hysteresis loop were shown at higher P/P0 indicating a flatter shape of pores (Al-Najar et al., 2017). The ZF-500 sample demonstrated larger adsorbed quantity (79 cm^3/g) in comparison to ZFO-600 (65 cm^3/g) and ZFO-700 (55 cm^3/g), respectively (**Figure 4a**). This indicates that ZFO-500 may possess a smaller pore diameter and higher surface area than other samples as shown in **Table TS2**. The calculated BET surface areas were recorded as 28.7 m^2/g for ZFO-500, 19 m^2/g for ZFO-600 and 14 m^2/g for ZFO-700, respectively. This matches well with our XRD and TEM results, where the increased grain and crystal sizes ,with increasing annealing temperature, lead to a lower surface area (Sun et al., 2020). Considering smaller grain/crystal size and large surface area of ZFO-500, it is expected to demonstrate excellent photocatalytic behavior.

3.5 Photocatalytic Response of ZFO nanoparticles

The photocatalytic activities for all ZFO samples were investigated for the degradation of MO and MB dyes in aqueous solution under simulated solar irradiation as shown in **Figures 4b and 4c**. No considerable dyes degradation was found in the absence of ZFO nanoparticles. However, ZFO samples demonstrated exceptional photocatalytic response to both dyes. The calculated MO dye degradation efficiencies were 84%, 56% and 54 % for ZFO-500, ZFO-600 and ZFO-700, respectively, within 120 minutes of reaction time.

Similar trend was observed for the degradation of MB dye and ZFO-500 showed highest degradation efficiency of 62% followed by ZFO-600 (52%) and ZFO-700 (46%) within the same reaction time. The overall dye degradation efficiencies of ZFO samples for MO dye (anionic) were superior than MB (cationic) dye. This may be attributed to the different chemical structure for the cationic and anionic dyes as they interact with ZFO surface using different functional chemical groups. Generally, the anionic dyes have a greater affinity toward the catalyst, which may be a potential reason for the high photodegradation efficiencies of ZFO samples toward anionic dyes (Trandafilović et al., 2017). In general, Spinel ferrite are considered as hydrophilic materials which have an isoelectric point (IEP) around pH = 7 (Bigham et al., 2018; Nguyen et al., 2019).

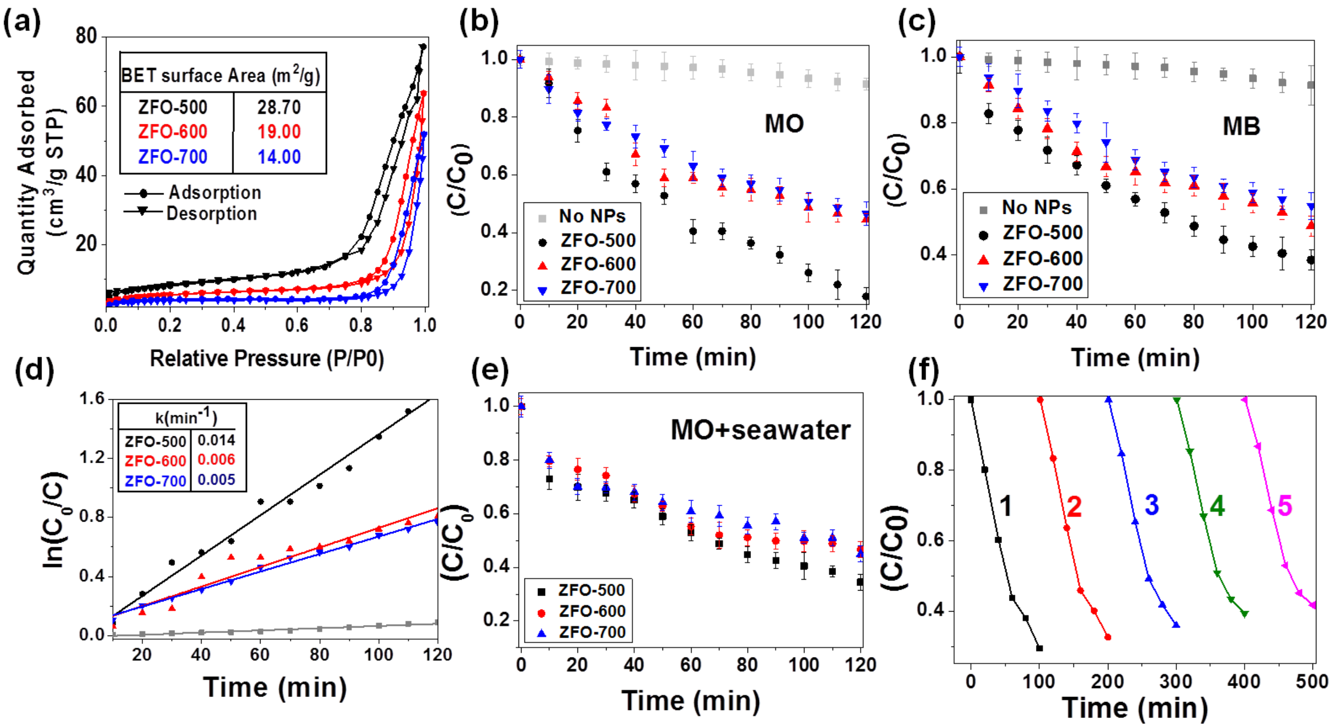

Figure 4: (a) The N2 adsorption-desorption isotherms curves and the calculated BET surface area (in the inset) for the ZFO samples prepared with different annealing temperatures (ZFO-500, ZFO-600 and ZFO-700) and their degradation curves of **(b)** MO dye in water, **(c)** MB dye in water under solar irradiation, **(d)** k-values for the MO dye degradation process in aqueous solution, **(e)** MO dye in sweater (pH= 8.15 and conductivity 32.45 mS) under solar irradiation, **(f)** MO dye degradation in aqueous solution over 5 repetitive cycles using ZFO-500.

The degradation of ZFO samples have shown a good alignment with the pseudo-first-order kinetic equation that given as:

$$\ln\left(\frac{C}{C_0}\right) = kt \qquad (2)$$

Where; C_0 is the initial absorbance of the dye solution, C is the absorbance of the dye solution at time (t) in (min), k is the first-order degradation rate constant (min^{-1}). The degradation rate kinetics of MO by fitting lines are shown in **Figure 4d**, where the calculated k values were recorded as 0.14, 0.006 and 0.005 min^{-1}. The ZFO-500 demonstrated highest k-value which exhibits the smallest particle size and highest surface area.

We further investigated the applicability of ZFO samples with MO dye in seawater and the results are depicted in **Figure 4e**. In spite of the tough chemical conditions of the seawater sample (pH= 8.15 and conductivity 32.45 mS), considerable degradation efficiencies ranging from 66%, 54% and 55% were recorded for ZFO-500, ZFO-600 and ZFO-700, respectively as shown in **Figure 4e**. To the best of our knowledge, limited efforts have been made to investigate the effect of nanoparticles in seawater photocatalysis. This could be mainly because most pollutants exist in lower concentration in seawater, in comparison with other resources. Also, seawater has higher pH and excessive ion concentration that disturb the photocatalysis process (T. Wang et al., 2019). However, the need of seawater treatment become more important nowadays because of the excessive use of desalinated water as a major freshwater source (Wang et al., 2018). Recently, a nanocomposite of $ZnO/ZnFe_2O_4$ have been utilized and only 10% degradation of MO in high pH condition (pH=8) within 140 min under visible light was recorded (Chandel et al., 2020). As per our knowledge, no previous reports have shown the effect of pure $ZnFe_2O_4$ nanoparticles in seawater photocatalysis. Our results are far superior than previous reports as ZFO-500 sample exhibited 66% degradation efficiencies of MO in seawater within two hours of reaction time.

To examine the reusability and durability of our ZFO-500 photocatalyst, a recycling study was carried out under identical conditions. As shown in **Figure 4f**, the reusability of

ZFO-500 photocatalyst was demonstrated up to a fifth cycle run and it is clearly observed that the nature of degradation remains unaltered and the inherent efficiency of ZFO-500 persisted (less than 5% decrease from its initial activity during the photodegradation process) without self-degradation. Also, **Figure S2** shows the XRD and the FTIR after the degradation process, confirming high stability of the ZFO-500 structure after the photocatalysis process. Therefore, our pure ZFO nanostructure (ZFO-500) possess relatively high degradation efficiencies for MO and MB dye, and could have great potential to be use for practical implications. ZFO-500 sample also exhibited good photocatalytic ability to degrade Phenol (64% at 120 min) as shown in **Figure S3**.

A comparison between our ZFO-500 sample and other related previous research where ferrites samples are used to determine degradation efficiencies of organic dyes is shown in **Table-1,** taking into consideration the applied irradiation and other experimental conditions such as pH and initial concentration of the catalyst. A pure phase $ZnFe_2O_4$ nannoparticles exhibited 38% of MO dye degradation under visible light (Chnadel et al., 2020). To obtain enhanced degradation efficiency, (Chnadel et al., 2020) have combined the $ZnFe_2O$ with other oxide and graphene, as well as applying lower pH (6) and more catalyst concentration (50 mg/100 mL) in comparison with this work. Other combined ferrites such as MnCo–Ferrite exhibited only 11 % for MO dye and 20 % for MB dye under UV irradiation (Yousefi-Mohammadi et al., 2018). Moreover, $Co_{0.5}Zn_{0.25}Ni_{0.25}$Fe2O4-$TiO_2$ nano-composite that have shown 60% degradation of MB dye within 120 min (Ciocarlan et al., 2018) while other ferrites composites showed 55 % form MB dye in 180 min under visible light (Mahdikhah et al., 2020). In general, photocatalysis experiment is highly influenced by the catalyst and by the surroundings (temperature and pH).

Table 1: Dye degradation efficiencies of nanoparticles applied in aqueous solution and in seawater photocatalysis under different parameters.

Nanoparticles	**Degradation Efficiency (%)**	**Irradiation**	**parameters (catalyst, time, pH)**	**Pollutant**	**Ref**
$ZnFe_2O_4$	35 %	UV	[catalyst] = 10 mgL, [Time] =160 min	MB	**(Gupta et al., 2020)**
$ZnFe_2O_4$	38%	visible light lamp	[catalyst] = 50 mg/100 mL [Time] =140 min, pH = 4.0	MO	(Chnadel et al., 2020)
ZnO/ZF/NG	10%	visible light lamp	[catalyst] = 50 mg/100 mL, [Time] =140 min, pH = 8	MO	(Chandel et al., 2020)
ZnO/ZF/NG	34%	visible light lamp	[catalyst] = 50 mg/100mL, [Time] =140 min, pH = 7	MO	(Chandel et al., 2020)
$ZnFe_2O_4$-Graphene	5%	visible light	[catalyst] = 1 mg/mL, [Time] =180 min	MO	(Ai et al., 2020)
$ZnFe_2O_4$-Graphene	56%	visible light	[catalyst] = 1 mg/mL, [Time] =180 min	MB	(Ai et al., 2020)
Mn-Co–Ferrite	11%	UV	[catalyst]=10 mg.L, [Time] =180 min	MO	(Yousefi-Mohammadi et al., 2018)
Mn-Co–Ferrite	20%	UV	[catalyst]=0.5 $g.L^{-1}$, [Time] =180 min	MB	(Yousefi-Mohammadi et al., 2018)
$Co_{0.5}Zn_{0.25}Ni_{0.25}Fe_2O_4$-$TiO_2$	30%	sim-Solar	[catalyst] = 1 g/L, [Time] =120 min	MO	(Ciocarlan et al., 2018)
$Co_{0.5}Zn_{0.25}Ni_{0.25}Fe_2O_4$-$TiO_2$	60%	sim-Solar	[catalyst] = 1 g/L, [Time] =120 min	MB	(Ciocarlan et al., 2018)
ZFO-500	84%	sim-Solar	[catalyst] = 10mg/100mL, [Time] =120 min – pH 7	MO	**This work**
ZFO-500	66%	sim-Solar	[catalyst] = 10mg/100mL, [Time] =120 min -seawater - pH 8.15, conductivity 32.45 mS	MO	**This work**

3.6 Mineralization capability of ZFO nanoparticles.

In order to investigate the mineralization capability of ZFO-500 sample, the percentage of total organic carbon (TOC) generation of MO dye was measured. **Figure 5a** shows the TOC generation and photo-degradation efficiency of MO solution over ZFO-500 under solar irradiation for 120 min. Clearly, MO degradation efficiency and TOC generation showed almost similar percentages during time reaching 82% and 73% at 120 min, respectively. This indicates that most of the photodegraded MO has been converted to CO_2, revealing a good mineralization capability of ZFO-500 sample during the photocatalysis process.

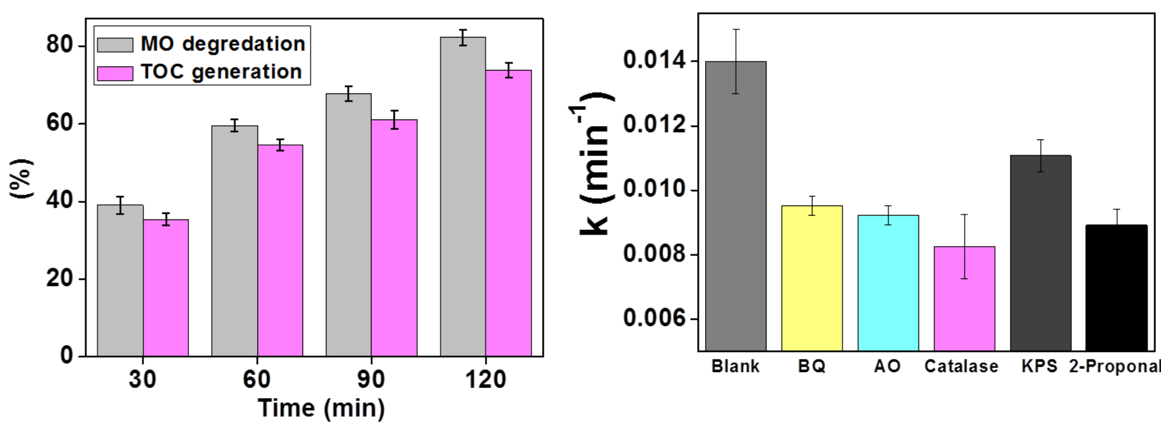

Figure 5: (a) Photocatalytic degradation efficiency and TOC percentage of MO of ZFo-500 under solar irradiation. (b) Effect of Benzoquinone (BQ) (6mmol/L), Ammonium Oxalate (AO)(0.05g/L), Catalase, (20mg/L), Potassium per Sulphate (KPS) (mmol/L) and 2-proponol (0.1 mmol/L) on the Rate constant (k) of MO degradation using ZFO-500 under solar irradiation.

3.7 Photocatalysis Mechanism and the role of Oxygen vacancies

The possible photo-degradation mechanism of MO and MB dyes under solar irradiation can be explained by the excitation of electrons from the valance band (VB) in ZFO atoms to its conduction band (CB). This could generate free electrons (e-) in CB and holes (h+) in VB which reacts with water molecules generating further ROS that cause chemical degradation to the dye. To further investigate the role of different ROS in the photocatalystics reaction, five ROS scavengers were applied in the photocatalysis process of MO using ZFO-500. These scavengers are Benzoquinone (BQ), Ammonium Oxalate (AO) Catalase, Potassium per Sulphate (KPS) and 2-proponol, which applied in scavenging Hydrogen peroxide (H_2O_2), holes (h+), Hydrogen peroxide (H_2O_2), electrons (e-) and Hydroxyl Radical (HO-), respectively. **Figure 5b** demonstrated the rate constant (k) of the degradation of MO with presence of these scavengers. The figure shows a considerable effect of all scavengers on the photocatalysis process. This indicates the involvement of the related ROS in the degradation of MO. The most effect is observed with Catalase, as the degradation constant (k) decreased from 0.015 min^{-1} to 0.008 min^{-1} indicating a major role of H_2O_2 in the MO degradation. The k value of other applied scavengers were calculated as follow; BQ=AO=2-propanol = 0.009 min^{-1} which indicates a similar role of h+ and OH- in the MO degradation that comes second after H_2O_2. The KPS, which is related to the e- contribution, revealed less change in k value (0.011 min^{-1}) in comparison with the pristine MO degradation (0.015 min^{-1}).

The following equations summaries the series of chemical reactions controlled by different ROS (Madhukara Naik et al., 2019).

$$ZnFe_2O_4 + hv(solar) \rightarrow ZnFe_2O_4(e^-_{CB} + h^+_{VB}) \quad (3)$$

$$ZnFe_2O_4(e^-_{CB}) + O_2 \rightarrow \cdot O_2^- \quad (4)$$

$$H_2O \rightarrow H^+ + HO^- \quad (5)$$

$$HO^- + h^+ \rightarrow HO^{\cdot} \quad (6)$$

$$\cdot O_2^- + H^+ \leftrightarrow HOO^{\cdot} \quad (7)$$

$$HOO^{\cdot} + e^{-} \rightarrow HOO^{-} \quad (8)$$

$$HOO^{-} + H^{+} \rightarrow H_2O_2 \quad (9)$$

$$H_2O_2 + e^{-} \rightarrow HO^{\cdot} + HO^{-} \quad (10)$$

$$ZnFe_2O_4(h_{VB}^{+}) + H_2O \rightarrow HO^{\cdot} + H^{+} \quad (11)$$

$$Dye + HO^{\cdot} \rightarrow CO_2 + H_2O(\text{By product}) \quad (12)$$

The holes can interact with hydroxyl ions in water generating hydroxyl radicals (OH·) as shown in equations 5 and 6, while superoxide radicals ($\cdot O_2^{-}$) are also created by the electrons react with oxygen molecules dissolved in water as shown in equations 7 and 8. These radicals create further oxidative reactions that form the reactive species hydroperoxyl radicals and hydrogen peroxide (H_2O_2), followed by the emerging of ($OH^{\cdot}$) radicals as shown in equations 9 and 10. Therefore, each ZFO nanoparticle will be surrounded with the created reactive species. Theses reactive species react with the organic dye molecules turning them to carbon dioxide and water molecules, which are less harmful than dye molecules (equation 11 and 12).

During the photocatalysis process, the electron-hole recombination rate is one of the main suppressors of the photocatalysis activity (Guo et al., 2014). More yields of electron-hole pairs will enhance the photocatalysis reactions, while the recombination would reduce the propensity of these reactions. Considering the ZFO samples, ZFO-500 has shown the greatest photocatalytic efficiencies in both types of dyes (MB an MO), in aqueous solution as well as in seawater. Along with the small size and high surface area of ZFO-500, the sufficiency of oxygen vacancies in its crystal lattice lead to a lower recombination rate and hence improved photocatalysis activity (Y. Huang et al., 2020).

Recent reports have revealed the strong correlation between oxygen vacancies and photocatalysis activity (Divya et al., 2020; Y. Huang et al., 2020; Sehar et al., 2021; Tan et al., 2014; Wan et al., 2020; F. Wang et al., 2017). The schematic diagram in **Figure 6** demonstrates a possible mechanism of the effect of oxygen vacancies in the energy levels of ZFO samples that in hence, affect their dye degradation efficiency. With more oxygen related defects, extra energy levels could be formed within the bandgap that cause longer pathways for electron transfer (i.e. slower recombination), in comparison with ZFO-600 and ZFO-700 (Afzal et al., 2020; Jaffari et al., 2012; Wan et al., 2020). In general, Oxygen vacancies could possibly enhance the photocatalysis activity through three mechanisms: (i) increasing light absorption capability (ii) reducing hole-electron recombination rate and (ii) increasing active sites on material surface (Y. Huang et al., 2020; Sehar et al., 2021; Wan et al., 2020; F. Wang et al., 2017). In our case, it can be anticipated that ZFO-500 exhibit high concentration of oxygen vacancies, thus, slow down the electron-hole recombination rates and availability of excessive active sites for dye molecules for reactions could be responsible for its excellent photocatalytic activities in comparison to ZFO-600 and ZFO-700 samples. The oxygen vacancies have been also related to the strong interaction between O_2 and semiconductor surface, which in turn facilitate the oxidation process that generates ROS (Y. Huang et al., 2020; Wan et al., 2020).

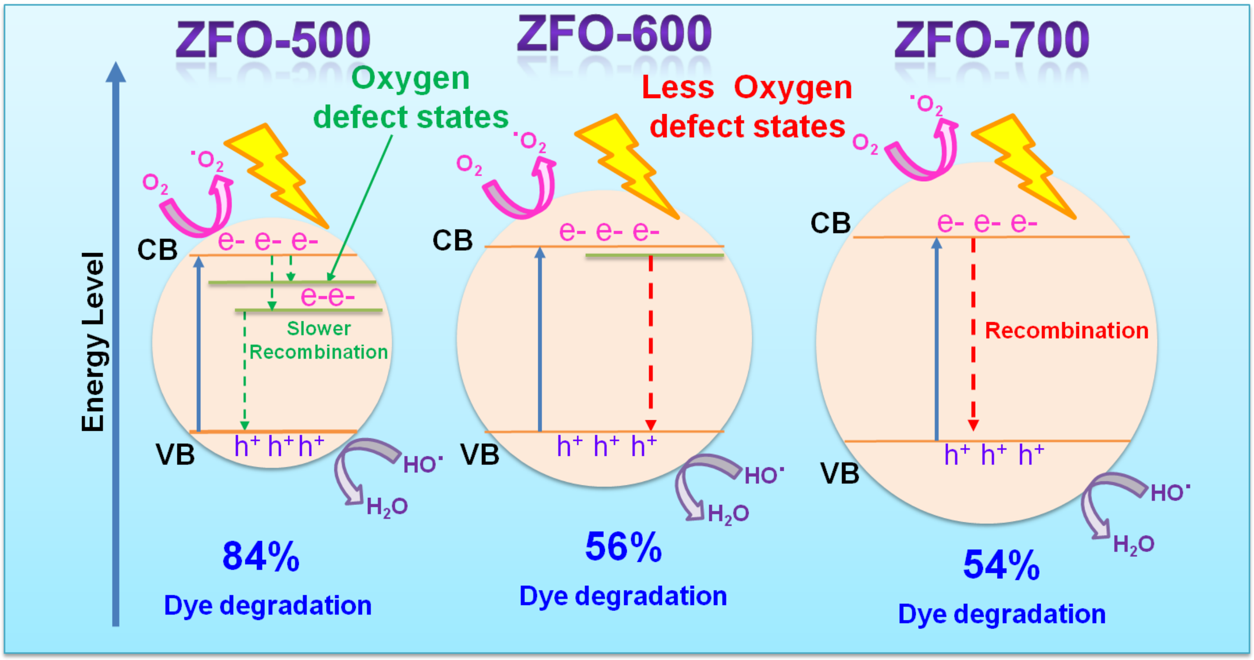

Figure 6: Schematic illustration of the photocatalysis process on the ZFO samples prepared using different annealing temperatures (ZFO-500, ZFO-600 and ZFO-700) showing the effect of Oxygen vacancies on electron-hole recombination.

3.8 Cytotoxicity assay of ZFO nanoparticles

The effect of ZFO nanoparticles were also examined on marine environment. Cytotoxicity assay were performed on the microalgae *Picochlorum sp.* by examining several factors as structure, viable cell concentrations, chlorophyll *a* concentration and reactive oxidative species (ROS) generation. Concentration experiment revealed that different concentration of ZFO-500 has no major effect on the number of viable cells during one week exposure. Previous research work also lessened the effect of concentration in viable cell counts (Bhuvaneshwari et al., 2015). Hence, 50 mg/L of ZFO samples was chosen for further investigations.

Figure 7a shows the structure of *Picochlorum sp*. using FTIR spectrum and three main bands at 3441, 1635 and 1111 cm^{-1} were found. The band at 3441 cm^{-1} may be related to the stretching of -NH and -OH bonds, lipids and proteins that construct the algae cell membrane. While the second band at 1635 cm^{-1} represents the stretching of C=O, protein amide. The third band may correspond to the Stretching of C-O-C, polysaccharides. After 4 weeks, the FTIR spectrum of the control algae cells was also monitored and no considerable shifts for its main peaks, nor additional peaks were identified, indicating a stable cell structure during the 4 weeks. As shown in **Figure 7a**, the addition of ZFO samples in the algae cells at a concentration of 50 mg/L for 4 weeks did not express any considerable changes on the bands intensities and the bands widths in the FTIR spectrum. This indicates that ZFO samples have no noticeable effect on the structure of *Picochlorum sp*. cells.

To further investigate the possible effects of ZFO samples on the *Picochlorum sp*. cells, viable cell counts were monitored weekly for all samples for four weeks. **Figure 7b** shows the decline of the viable cell concentration of the control algae sample as well as the algae/ZFO samples. The decline of the viable cell concentration is expected to be a part of the algae cells cycle starting from exponential growth phase, stationary phase and decline phase. **Figure 7b** demonstrates that all samples have been through the same rhythm of viable cell decline through the four weeks. Furthermore, ANOVA statistical test revealed that there is no significant difference in the decline rate between the control sample and other ZFO samples all over the four weeks.

The Chlorophyll *a* concentration was also calculated for all algae/ZFO samples for a period of four weeks. **Figure 7c** demonstrates that there is no obvious difference between the Chlorophyll *a* concentration in the control sample and algae/ZFO for 4 weeks which are consistence with viable cell results. ANOVA test also confirm that there is no significant statistical variation between the samples. Based on these results, there is no evidence that our prepared ZFO samples could cause a major effect on the *Picochlorum sp. cell* regeneration as well as their function in Chlorophyll *a* production.

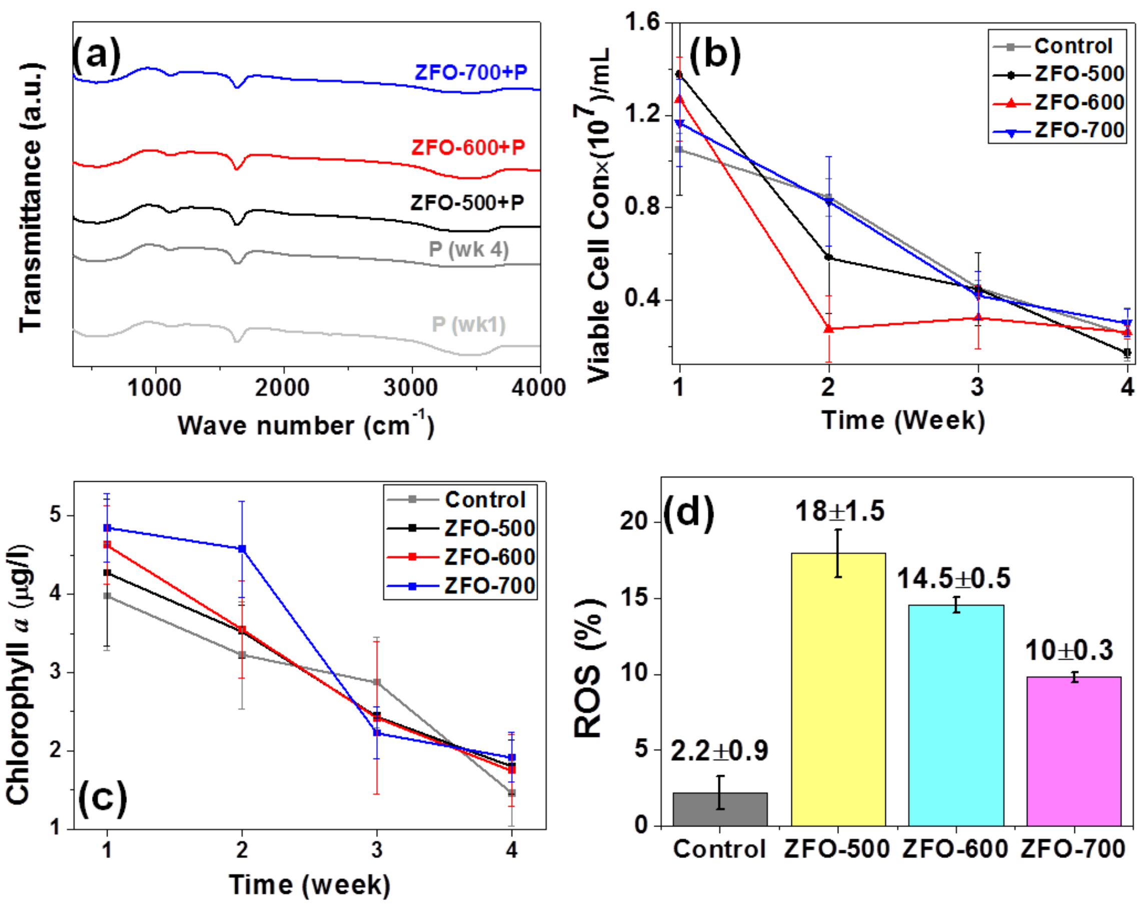

Figure 7: The cytotoxicity effect of ZFO samples synthesized using different annealing temperatures (ZFO-500, ZFO-600 and ZFO-700) applying (a) Fourier-transform infrared spectroscopy (FTIR) (b) Viable cells count (c) Chlorophyll *a* concentration and (d)Reactive Oxygen species (ROS) percentage after four weeks.

To assess whether the ZFO exposure to *Picochlorum sp.* caused any possible stress, the ROS generation percentage were measured in week 4. As shown in **Figure 7d**, the ROS percentage increased from 3% for the control algae sample to 18, 15 and 10% for ZFO-500, ZFO-600 and ZFO-700, respectively. ANOVA test has confirmed that such change in ROS percentage is statistically significant. This indicates that the existence of the ZFO nanoparticles created some disturbance to the *Picochlorum sp.* cells with the highest percentage related to ZFO-500. This variation in ROS generation upon the ZFO samples can be explained by their different sizes as the size of nanoparticles is reported to have a major effect on the cytotoxicty on fresh water algae *Scenedesmus obliquus* (Bhuvaneshwari et al., 2015). Also, Zhang et al (Zhang et al., 2016) have shown that nano sized ZnO particles demonstrated more toxic effects on marine microalgae *Skeletonema costatum* when compared with bulk-ZnO.

Overall, our ZFO samples can be considered as eco-friendly material to *Picochlorum sp.* marine algae. More investigation in other types of marine algae would strengthen this proposition. Considering the size of nanoparticles as an important enhancer of photocatalysis activity, it is essential to optimize the catalyst toxicity to environment, especially if it has potential to be applied in actual wastewater treatment processes that might result in direct contact with marine environment.

Conclusions

In summary, we reported modulation in oxygen vacancies in ZFO with the aid of thermal annealing to achieve excellent organic dye degradation efficiencies in aqueous solution and in seawater. To alter the abundance of oxygen vacancies in ZFO lattice, the samples were heated at three different temperatures (500, 600 and 700°C). This was confirmed from different characteristic modalities that investigated the crystal structure, surface area, optical absorption and emission. Samples annealed at 500°C showed superior photocatalytic dye degradation abilities in aqueous solution and also in seawater. Cytotoxicity tests confirmed insignificant effect of prepared samples on marine micro algae *Picochlorum sp* cell structure and Chlorophyll *a* production. These characteristics make our ZFO sample a good candidate for efficient wastewater treatment in different conditions without causing harmful consequences to environmental eco-system. Thus far, investigations are essential on boarder marine culture. Further study in photocatalysis process design and parameters is also essential.

Acknowledgement

We would like to extend our appreciation to:

- National Mariculture Centre, Ministry of Municipalities and Urban Planning, Kingdom of Bahrain, for providing *Picoplankton Picochlorum sp* culture samples.
- Mr. Manohar E Reddy from ExpressMed Labs- Kingdom of Bahrain, for taking TEM images of ZFO samples.
- Mrs. Muneera Almeshkhas from the Department of Chemistry – College of Science University of Bahrain for assisting FTIR measurements for ZFO and ZFO/algae samples.

References

Abdullah, N., Othman, F.E.C., Yusof, N., Matsuura, T., Lau, W.J., Jaafar, J., Ismail, A.F., Salleh, W.N.W., Aziz, F., 2020. Preparation of nanocomposite activated carbon nanofiber/manganese oxide and its adsorptive performance toward leads (II) from aqueous solution. J. Water Process Eng. 37, 101430. https://doi.org/10.1016/j.jwpe.2020.101430

Afzal, A., Mujahid, A., Iqbal, N., Javaid, R., 2020. Enhanced High-Temperature (600 ◦ C) NO 2 Response of ZnFe 2 O 4 Nanoparticle-Based Exhaust Gas Sensors 3, 1–14.

Ai, J., Hu, L., Zhou, Z., Cheng, L., Liu, W., Su, K., Zhang, R., Chen, Z., Li, W., 2020. Surfactant-free synthesis of a novel octahedral ZnFe2O4/graphene composite with high adsorption and good photocatalytic activity for efficient treatment of dye wastewater. Ceram. Int. 46, 11786–11798. https://doi.org/10.1016/j.ceramint.2020.01.213

Al-Najar, B., Khezami, L., Judith Vijaya, J., Lemine, O.M., Bououdina, M., 2017. Effect of synthesis route on the uptake of Ni and Cd by MgFe2O4 nanopowders. Appl. Phys. A Mater. Sci. Process. 123, 1–8. https://doi.org/10.1007/s00339-016-0710-7

Al-Najar, B., Peters, C.D., Albuflasa, H., Hankins, N.P., 2020. Pressure and osmotically driven membrane processes: A review of the benefits and production of nano-enhanced membranes for desalination. Desalination 479, 114323. https://doi.org/10.1016/J.DESAL.2020.114323

Amir, M., Gungunes, H., Baykal, A., Almessiere, M.A., Sözeri, H., Ercan, I., Sertkol, M., Asiri, S., Manikandan, A., 2018. Effect of Annealing Temperature on Magnetic and Mössbauer Properties of ZnFe2O4 Nanoparticles by Sol-gel Approach. J. Supercond. Nov. Magn. 31, 3347–3356. https://doi.org/10.1007/s10948-018-4610-2

Amiri, M., Gholami, T., Amiri, O., Pardakhti, A., Ahmadi, M., Akbari, A., Amanatfard, A., Salavati-Niasari, M., 2020. The magnetic inorganic-organic nanocomposite based on ZnFe2O4-Imatinib-liposome for biomedical applications, in vivo and in vitro study. J. Alloys Compd. 849, 156604. https://doi.org/10.1016/j.jallcom.2020.156604

Arora, I., Sharma, P.K., 2021. Characterization of oxygen vacancy effect on structure and optoelectronic properties of sol gel deposited Zn2-xCaxSnO4 nanostructured films. Mater. Chem. Phys. 258, 123905. https://doi.org/10.1016/j.matchemphys.2020.123905

Baynosa, M.L., Mady, A.H., Nguyen, V.Q., Kumar, D.R., Sayed, M.S., Tuma, D., Shim, J.J., 2020. Eco-friendly synthesis of recyclable mesoporous zinc ferrite@reduced graphene oxide nanocomposite for efficient photocatalytic dye degradation under solar radiation. J. Colloid Interface Sci. 561, 459–469. https://doi.org/10.1016/j.jcis.2019.11.018

Bhushan Das, S., Kumar Singh, R., Kumar, V., Kumar, N., Kumar, S., 2021. Tailoring the structural, optical and multiferroic properties of low temperature synthesized cobalt ferrite nanomaterials, by citrate precursor method. Mater. Today Proc. 1–7. https://doi.org/10.1016/j.matpr.2021.04.001

Bhuvaneshwari, M., Iswarya, V., Archanaa, S., Madhu, G.M., Kumar, G.K.S., Nagarajan, R., Chandrasekaran, N., Mukherjee, A., 2015. Cytotoxicity of ZnO NPs towards fresh water algae Scenedesmus obliquus at low exposure concentrations in UV-C, visible and dark conditions. Aquat. Toxicol. 162, 29–38. https://doi.org/10.1016/j.aquatox.2015.03.004

Bigham, A., Foroughi, F., Motamedi, M., Rafienia, M., 2018. Multifunctional nanoporous magnetic zinc silicate-ZnFe2O4 core-shell composite for bone tissue engineering applications. Ceram. Int. 44, 11798–11806. https://doi.org/10.1016/j.ceramint.2018.03.264

Chandel, N., Sharma, K., Sudhaik, A., Raizada, P., Hosseini-Bandegharaei, A., Thakur, V.K., Singh, P., 2020. Magnetically separable $ZnO/ZnFe_2O_4$ and $ZnO/CoFe_2O_4$ photocatalysts supported onto nitrogen doped graphene for photocatalytic degradation of toxic dyes. Arab. J. Chem. 13, 4324–4340. https://doi.org/10.1016/j.arabjc.2019.08.005

Chen, P., Hu, X., Qi, Y., Wang, X., Li, Z., Zhao, L., Liu, S., Cui, C., 2017. Rapid degradation of azo dyes by melt-spun Mg-Zn-Ca metallic glass in artificial seawater. Metals (Basel). 7. https://doi.org/10.3390/met7110485

Chiu, Y.-H., Chang, T.-F.M., Chen, C.-Y., Sone, M., Hsu, Y.-J., 2019. Mechanistic Insights into Photodegradation of Organic Dyes Using Heterostructure Photocatalysts. Catal. . https://doi.org/10.3390/catal9050430

Chnadel, N., Dutta, V., Sharma, S., Raizada, P., Sonu, Hosseini-Bandegharaei, A., Kumar, R., Singh, P., Thakur, V.K., 2020. Z-scheme photocatalytic dye degradation on $AgBr/Zn(Co)Fe_2O_4$ photocatalysts supported on nitrogen-doped graphene. Mater. Today Sustain. 9, 100043. https://doi.org/10.1016/j.mtsust.2020.100043

Ciocarlan, R.G., Seftel, E.M., Mertens, M., Pui, A., Mazaj, M., Novak Tusar, N., Cool, P., 2018. Novel magnetic nanocomposites containing quaternary ferrites systems $Co_{0.5}Zn_{0.25}M_{0.25}Fe_2O_4$ (M = Ni, Cu, Mn, Mg) and TiO_2-anatase phase as photocatalysts for wastewater remediation under solar light irradiation. Mater. Sci. Eng. B Solid-State Mater. Adv. Technol. 230, 1–7.

https://doi.org/10.1016/j.mseb.2017.12.030

Dang, H., Qiu, Y., Cheng, Z., Yang, W., Wu, H., Fan, H., Dong, X., 2016. Hydrothermal preparation and characterization of nanostructured CNTs/ZnFe2O4 composites for solar water splitting application. Ceram. Int. 42, 10520–10525. https://doi.org/10.1016/j.ceramint.2016.03.019

Deka, D.J., Gunduz, S., Fitzgerald, T., Miller, J.T., Co, A.C., Ozkan, U.S., 2019. Production of syngas with controllable H2/CO ratio by high temperature co-electrolysis of CO2 and H2O over Ni and Co- doped lanthanum strontium ferrite perovskite cathodes. Appl. Catal. B Environ. 248, 487–503. https://doi.org/https://doi.org/10.1016/j.apcatb.2019.02.045

Dippong, T., Cadar, O., Deac, I.G., Lazar, M., Borodi, G., Levei, E.A., 2020. Influence of ferrite to silica ratio and thermal treatment on porosity, surface, microstructure and magnetic properties of Zn0.5Ni0.5Fe2O4/SiO2 nanocomposites. J. Alloys Compd. 828, 154409. https://doi.org/10.1016/j.jallcom.2020.154409

Dippong, T., Deac, I.G., Cadar, O., Levei, E.A., Diamandescu, L., Borodi, G., 2019. Effect of Zn content on structural, morphological and magnetic behavior of ZnxCo1-xFe2O4/SiO2 nanocomposites. J. Alloys Compd. 792, 432–443. https://doi.org/10.1016/j.jallcom.2019.04.059

Divya, J., Shivaramu, N.J., Purcell, W., Roos, W.D., Swart, H.C., 2020. Effects of annealing temperature on the crystal structure, optical and photocatalytic properties of Bi2O3 needles. Appl. Surf. Sci. 520, 146294. https://doi.org/10.1016/j.apsusc.2020.146294

El-naggar, A.M., Mohamed, M.B., Aldhafiri, A.M., Heiba, Z.K., 2020. Effect of vacancies and vanadium doping on the structural and magnetic properties of nano $LiFe_{2.5}O_4$. J. Mater. Res. Technol. 9, 16435–16444. https://doi.org/10.1016/j.jmrt.2020.11.097

Fu, L., Zhou, J., Zhou, L., Yang, J., Liu, Z., Wu, Ke, Zhao, H., Wang, J., Wu, Kai, 2021. Facile fabrication of exsolved nanoparticle-decorated hollow ferrite fibers as active electrocatalyst for oxygen evolution reaction. Chem. Eng. J. 418, 129422. https://doi.org/https://doi.org/10.1016/j.cej.2021.129422

Guo, X., Zhu, H., Li, Q., 2014. Visible-light-driven photocatalytic properties of $ZnO/ZnFe_2O_4$ core/shell nanocable arrays. Appl. Catal. B Environ. 160–161, 408–414. https://doi.org/10.1016/j.apcatb.2014.05.047

Gupta, N.K., Ghaffari, Y., Kim, S., Bae, J., Kim, K.S., Saifuddin, M., 2020. Photocatalytic Degradation of Organic Pollutants over MFe_2O_4 (M = Co, Ni, Cu, Zn) Nanoparticles at Neutral pH. Sci. Rep. 10, 1–11. https://doi.org/10.1038/s41598-020-61930-2

Hashemi, S.H., Kaykhaii, M., Jamali Keikha, A., Mirmoradzehi, E., 2019. Box-Behnken design optimization of pipette tip solid phase extraction for methyl orange and acid red determination by spectrophotometry in seawater samples using graphite based magnetic NiFe 2 O 4 decorated exfoliated as sorbent. Spectrochim. Acta - Part A Mol. Biomol. Spectrosc. 213, 218–227. https://doi.org/10.1016/j.saa.2019.01.049

Hazeem, L.J., Bououdina, M., Rashdan, S., Brunet, L., Slomianny, C., Boukherroub, R., 2016. Cumulative effect of zinc oxide and titanium oxide nanoparticles on growth and chlorophyll a content of Picochlorum sp. Environ. Sci. Pollut. Res. 23, 2821–2830. https://doi.org/10.1007/s11356-015-5493-4

Huang, J., Zimmerman, A.R., Chen, H., Gao, B., 2020. Ball milled biochar effectively removes sulfamethoxazole and sulfapyridine antibiotics from water and wastewater. Environ. Pollut. 258, 113809. https://doi.org/10.1016/j.envpol.2019.113809

Huang, Y., Yu, Yu, Yu, Yifu, Zhang, B., 2020. Oxygen Vacancy Engineering in Photocatalysis. Sol. RRL 4, 1–14. https://doi.org/10.1002/solr.202000037

Jaffari, G.H., Rumaiz, A.K., Woicik, J.C., Shah, S.I., 2012. Influence of oxygen vacancies on the electronic structure and magnetic properties of NiFe 2O 4 thin films. J. Appl. Phys. 111. https://doi.org/10.1063/1.4704690

Khadgi, N., Upreti, A.R., 2019. Photocatalytic degradation of Microcystin-LR by visible light active and magnetic, ZnFe2O4-Ag/rGO nanocomposite and toxicity assessment of the intermediates. Chemosphere 221, 441–451. https://doi.org/10.1016/j.chemosphere.2019.01.046

Lei, B., Cui, W., Sheng, J., Wang, H., Chen, P., Li, J., Sun, Y., Dong, F., 2020. Synergistic effects of crystal structure and oxygen vacancy on Bi2O3 polymorphs: intermediates activation, photocatalytic reaction efficiency, and conversion pathway. Sci. Bull. 65, 467–476. https://doi.org/10.1016/j.scib.2020.01.007

Madhukara Naik, M., Bhojya Naik, H.S., Nagaraju, G., Vinuth, M., Raja Naika, H., Vinu, K., 2019. Green synthesis of zinc ferrite nanoparticles in Limonia acidissima juice: Characterization and their application as photocatalytic and antibacterial activities. Microchem. J. 146, 1227–1235. https://doi.org/10.1016/j.microc.2019.02.059

Mahdikhah, V., Saadatkia, S., Sheibani, S., Ataie, A., 2020. Outstanding photocatalytic activity of CoFe2O4 /rGO nanocomposite in degradation of organic dyes. Opt. Mater. (Amst). 108, 110193. https://doi.org/10.1016/j.optmat.2020.110193

Mahy, J.G., Wolfs, C., Mertes, A., Vreuls, C., Drot, S., Smeets, S., Dircks, S., Boergers, A., Tuerk, J., Lambert, S.D., 2019. Advanced photocatalytic oxidation processes for micropollutant elimination from municipal and industrial water. J. Environ. Manage. 250, 109561. https://doi.org/10.1016/j.jenvman.2019.109561

Mana, R., Raguram, T., Rajni, K.S., 2019. Physical properties of nickel ferrite nanoparticles at different annealing temperature prepared by sol-gel technique. Mater. Today Proc. 18, 1753–1759. https://doi.org/10.1016/j.matpr.2019.05.274

Manikandan, A., Kennedy, L.J., Bououdina, M., Vijaya, J.J., 2014. Synthesis, optical and magnetic properties of pure and Co-doped ZnFe 2O4 nanoparticles by microwave combustion method. J. Magn. Magn. Mater. 349, 249–258. https://doi.org/10.1016/j.jmmm.2013.09.013

Naseri, M., Kamalianfar, A., Naderi, E., Hashemi, A., 2020. The effect of Ag nanoparticles on physical and photocatalytic properties of ZnFe2O4/SiO2 nanocomposite. J. Mol. Struct. 1206, 127706. https://doi.org/10.1016/j.molstruc.2020.127706

Nguyen, T.B., Huang, C.P., Doong, R. an, 2019. Photocatalytic degradation of bisphenol A over a ZnFe 2 O 4 /TiO 2 nanocomposite under visible light. Sci. Total Environ. 646, 745–756. https://doi.org/10.1016/j.scitotenv.2018.07.352

Peng, S., Wang, Z., Liu, R., Bi, J., Wu, J., 2019. Controlled oxygen vacancies of ZnFe2O4 with superior gas sensing properties prepared via a facile one-step self-catalyzed treatment. Sensors Actuators, B Chem. 288, 649–655. https://doi.org/10.1016/j.snb.2019.03.056

Porcar-Santos, O., Cruz-Alcalde, A., López-Vinent, N., Zanganas, D., Sans, C., 2020. Photocatalytic degradation of sulfamethoxazole using TiO2 in simulated seawater: Evidence for direct formation of reactive halogen species and halogenated by-products. Sci. Total Environ. 736, 139605. https://doi.org/https://doi.org/10.1016/j.scitotenv.2020.139605

Prasad, C., Liu, Q., Tang, H., Yuvaraja, G., Long, J., Rammohan, A., Zyryanov, G. V., 2020. An overview of graphene oxide supported semiconductors based photocatalysts: Properties, synthesis and photocatalytic applications. J. Mol. Liq. 297, 111826. https://doi.org/10.1016/j.molliq.2019.111826

Qin, M., Shuai, Q., Wu, G., Zheng, B., Wang, Z., Wu, H., 2017. Zinc ferrite composite material with controllable morphology and its applications. Mater. Sci. Eng. B Solid-State Mater. Adv. Technol. 224, 125–138. https://doi.org/10.1016/j.mseb.2017.07.016

Qureshi, A.S., 2020. Challenges and Prospects of Using Treated Wastewater to Manage Water Scarcity Crises in the. Water J. 12, 1–16.

Radhakrishnan, A., Rejani, P., Khan, J.S., Beena, B., 2016. Ecotoxicology and Environmental Safety Effect of annealing on the spectral and optical characteristics of nano ZnO : Evaluation of adsorption of toxic metal ions from industrial waste water. Ecotoxicol. Environ. Saf. 133, 457–465. https://doi.org/10.1016/j.ecoenv.2016.08.001

Rashdan, S.A., Hazeem, L.J., 2020. Synthesis of spinel ferrites nanoparticles and investigating their effect on the growth of microalgae Picochlorum sp. Arab J. Basic Appl. Sci. 27, 134–141. https://doi.org/10.1080/25765299.2020.1733174

Sapna, Budhiraja, N., Kumar, V., Singh, S.K., 2019. Shape-controlled synthesis of superparamagnetic ZnFe2O4 hierarchical structures and their comparative structural, optical and magnetic properties. Ceram. Int. 45, 1067–1076. https://doi.org/10.1016/j.ceramint.2018.09.286

Sarkar, A., Khan, G.G., 2019. The formation and detection techniques of oxygen vacancies in titanium oxide-based nanostructures. Nanoscale 11, 3414–3444. https://doi.org/10.1039/c8nr09666j

Sehar, S., Naz, I., Perveen, I., Ahmed, S., 2019. Superior dye degradation using SnO2-ZnO hybrid heterostructure catalysts. Korean J. Chem. Eng. 36, 56–62. https://doi.org/10.1007/s11814-018-0159-9

Sehar, S., Naz, I., Rehman, A., Sun, W., Alhewairini, S.S., Zahid, M.N., Younis, A., 2021. Shape-controlled synthesis of cerium oxide nanoparticles for efficient dye photodegradation and antibacterial activities. Appl. Organomet. Chem. 35, e6069. https://doi.org/https://doi.org/10.1002/aoc.6069

Serpone, N., 2018. Heterogeneous photocatalysis and prospects of TiO2-based photocatalytic DeNOxing the atmospheric environment. Catalysts 8. https://doi.org/10.3390/catal8110553

Sert, G., Bunani, S., Yörükoğlu, E., Kabay, N., Egemen, Ö., Arda, M., Yüksel, M., 2017. Performances of some NF and RO membranes for desalination of MBR treated wastewater. J. Water Process Eng. 16, 193–198. https://doi.org/10.1016/j.jwpe.2016.11.009

Shah, J., Jain, S., Gahtori, B., Sharma, C., Kotnala, R.K., 2021. Water splitting on the mesoporous surface and oxygen vacancies of iron oxide generates electricity by hydroelectric cell. Mater. Chem. Phys. 258, 123981. https://doi.org/10.1016/j.matchemphys.2020.123981

Sun, K.M., Song, X.Z., Wang, X.F., Li, X., Tan, Z., 2020. Annealing temperature-dependent porous ZnFe2O4 olives derived from bimetallic organic frameworks for high-performance ethanol gas sensing. Mater. Chem. Phys. 241, 2–7. https://doi.org/10.1016/j.matchemphys.2019.122379

Surendra, B.S., Shashi Shekhar, T.R., Veerabhadraswamy, M., Nagaswarupa, H.P., Prashantha, S.C., Geethanjali, G.C., Likitha, C., 2020. Probe sonication synthesis of ZnFe2O4 NPs for the photocatalytic degradation of dyes and effect of treated wastewater on growth of plants. Chem. Phys. Lett. 745, 137286. https://doi.org/10.1016/j.cplett.2020.137286

Swathi, S., Yuvakkumar, R., Kumar, P.S., Ravi, G., Velauthapillai, D., 2021. Annealing temperature effect on cobalt ferrite nanoparticles for photocatalytic degradation. Chemosphere 281, 130903. https://doi.org/10.1016/j.chemosphere.2021.130903

Tan, H., Zhao, Z., Zhu, W., Coker, E.N., Li, B., Zheng, M., Yu, W., Fan, H., Sun, Z., 2014. Oxygen Vacancy Enhanced Photocatalytic Activity of Pervoskite SrTiO3. ACS Appl. Mater. Interfaces 6, 19184–19190. https://doi.org/10.1021/am5051907

Tkaczyk, A., Mitrowska, K., Posyniak, A., 2020. Synthetic organic dyes as contaminants of the aquatic environment and their implications for ecosystems: A review. Sci. Total Environ. 717, 137222. https://doi.org/10.1016/j.scitotenv.2020.137222

Trandafilović, L. V., Jovanović, D.J., Zhang, X., Ptasińska, S., Dramićanin, M.D., 2017. Enhanced photocatalytic degradation of methylene blue and methyl orange by ZnO:Eu nanoparticles. Appl. Catal. B Environ. 203, 740–752. https://doi.org/10.1016/j.apcatb.2016.10.063

Vinosha, P.A., Mely, L.A., Jeronsia, J.E., Krishnan, S., Das, S.J., 2017. Synthesis and properties of spinel ZnFe2O4 nanoparticles by facile co-precipitation route. Optik (Stuttg). 134, 99–108. https://doi.org/10.1016/j.ijleo.2017.01.018

Wan, Z., Hu, M., Hu, B., Yan, T., Wang, K., Wang, X., 2020. Vacancy induced photocatalytic activity of la doped In(OH)3 for CO2 reduction with water vapor. Catal. Sci. Technol. 10, 2893–2904. https://doi.org/10.1039/d0cy00029a

Wang, F., Chen, D., Zhang, N., Wang, S., Qin, L., Sun, X., Huang, Y., 2017. Oxygen vacancies induced by zirconium doping in bismuth ferrite nanoparticles for enhanced photocatalytic performance. J. Colloid Interface Sci. 508, 237–247. https://doi.org/https://doi.org/10.1016/j.jcis.2017.08.056

Wang, J., Wang, Y., Xv, X., Chen, Y., Yang, X., Zhou, J., Li, S., Cao, F., Qin, G., 2019. Defective Fe3+ self-doped spinel ZnFe2O4 with oxygen vacancies for highly efficient photoelectrochemical water splitting. Dalt. Trans. 48, 11934–11940. https://doi.org/10.1039/c9dt01033e

Wang, Q., Cai, C., Wang, M., Guo, Q., Wang, B., Luo, W., Wang, Y., Zhang, C., Zhou, L., Zhang, D., Tong, Z., Liu, Y., Chen, J., 2018. Efficient photocatalytic degradation of Malachite Green in seawater by the hybrid of Zinc-Oxide Nanorods Grown on Three-Dimensional (3D) reduced graphene oxide(RGO)/Ni foam. Materials (Basel). 11. https://doi.org/10.3390/ma11061004

Wang, T., Xu, Z.Y., Wu, L.G., Li, B.R., Chen, M.X., Xue, S.Y., Zhu, Y.C., Cai, J., 2017. Enhanced photocatalytic activity for degrading phenol in seawater by TiO2-based catalysts under weak light irradiation. RSC Adv. 7, 31921–31929. https://doi.org/10.1039/c7ra04732k

Wang, T., Zhang, Y. ling, Pan, J. hao, Li, B. rui, Wu, L. guang, Jiang, B. qiong, 2019. Hydrothermal reduction of commercial P25 photocatalysts to expand their visible-light response and enhance their performance for photodegrading phenol in high-salinity wastewater. Appl. Surf. Sci. 480, 896–904. https://doi.org/10.1016/j.apsusc.2019.03.052

Wang, Yujing, Song, H., Chen, J., Chai, S., Shi, L., Chen, C., Wang, Yanbin, He, C., 2020. A novel solar photo-Fenton system with self-synthesizing H2O2: Enhanced photo-induced catalytic performances and mechanism insights. Appl. Surf. Sci. 512, 145650. https://doi.org/10.1016/j.apsusc.2020.145650

Wu, K., Li, J., Zhang, C., 2019. Zinc ferrite based gas sensors: A review. Ceram. Int. 45, 11143–11157. https://doi.org/10.1016/j.ceramint.2019.03.086

Yadav, N.G., Chaudhary, L.S., Sakhare, P.A., Dongale, T.D., Patil, P.S., Sheikh, A.D., 2018. Impact of collected sunlight on ZnFe2O4 nanoparticles for photocatalytic application. J. Colloid Interface Sci. 527, 289–297. https://doi.org/10.1016/j.jcis.2018.05.051

Yentür, G., Dükkancı, M., 2020. Fabrication of magnetically separable plasmonic composite photocatalyst of Ag/AgBr/ZnFe2O4 for visible light photocatalytic oxidation of carbamazepine. Appl. Surf. Sci. 510, 145374. https://doi.org/10.1016/j.apsusc.2020.145374

Younis, A., Chu, D., Kaneti, Y.V., Li, S., 2016. Tuning the surface oxygen concentration of {111} surrounded ceria nanocrystals for enhanced photocatalytic activities. Nanoscale 8, 378–387. https://doi.org/10.1039/c5nr06588g

Younis, A., Loucif, A., 2021. Defects mediated enhanced catalytic and humidity sensing performance in ceria nanorods. Ceram. Int. 47, 15500–15507. https://doi.org/https://doi.org/10.1016/j.ceramint.2021.02.117

Younis, A., Shirsath, S.E., Shabbir, B., Li, S., 2018. Controllable dynamics of oxygen vacancies through extrinsic doping for superior catalytic activities. Nanoscale 10, 18576–18585. https://doi.org/10.1039/C8NR03801E

Yousefi-Mohammadi, S., Movahedi, M., Salavati, H., 2018. MnCo–Ferrite/TiO2 composite as an efficient magnetically separable photocatalyst for decolorization of dye pollutants in aqueous solution. Surfaces and Interfaces 11, 91–97. https://doi.org/10.1016/j.surfin.2018.03.004

Zhang, C., Wang, J., Tan, L., Chen, X., 2016. Toxic effects of nano-ZnO on marine microalgae Skeletonema costatum: Attention to the accumulation of intracellular Zn.

Aquat. Toxicol. 178, 158–164. https://doi.org/10.1016/j.aquatox.2016.07.020

Zhang, H., Li, C., Lyu, L., Hu, C., 2020. Surface oxygen vacancy inducing peroxymonosulfate activation through electron donation of pollutants over cobalt-zinc ferrite for water purification. Appl. Catal. B Environ. 270, 118874. https://doi.org/10.1016/j.apcatb.2020.118874